Composites Part B 217 (2021) 108912

Contents lists available at ScienceDirect

Composites Part B

journal homepage: www.elsevier.com/locate/compositesb

Enhancing strength-ductility synergy and mechanisms of Al-based composites by size-tunable in-situ TiB_2 particles with specific spatial distribution

Bai-Xin Dong [a,b], Qiang Li [a,b], Zhi-Fa Wang [a,b], Tian-Shu Liu [a,b], Hong-Yu Yang [a,b,e,*], Shi-Li Shu [a,d], Liang-Yu Chen [e], Feng Qiu [a,b], Qi-Chuan Jiang [a,b], Lai-Chang Zhang [c]

[a] State Key Laboratory of Automotive Simulation and Control, Jilin University, PR China
[b] Key Laboratory of Automobile Materials, Ministry of Education and Department of Materials Science and Engineering, Jilin University, Renmin Street No. 5988, Changchun, Jilin Province, 130025, PR China
[c] School of Engineering, Edith Cowan University, 270 Joondalup Drive, Joondalup, Perth, WA, 6027, Australia
[d] School of Mechanical and Aerospace Engineering, Jilin University, Renmin Street No. 5988, Changchun, Jilin Province, 130025, PR China
[e] School of Materials Science and Engineering, Jiangsu University of Science and Technology, Zhenjiang, 212003, PR China

ARTICLE INFO

Keywords:
Enhancing strength-ductility synergy
TiB_2 particles
Size and morphology tuning
Al/TiB_2 interface
Spatial distribution

ABSTRACT

The increase in strength usually accompanies by the sacrifice of ductility in the composites. This work proposed a strategy of design and synthesis of in-situ TiB_2 particles to effectively tailor the microstructures and to enhance the mechanical performance of Al–Si-based composites. The tuning mechanisms for size and morphology of TiB_2 particles were investigated by combustion synthesis in the Al–Ti–B reaction system. The nano/submicron-sized TiB_2 particles with desirable morphology were then specially selected to construct high-performance Al–Si-based composites. Thanks to the strong interface bonding with a low crystallographic mismatch, TiB_2 particles significantly refined the primary α-Al dendrites, eutectic Si and θ' precipitates in the composites, which were 79.2%, 51.9% and 37.6% respectively smaller than those of the matrix. Numerical modeling results suggested that submicron-sized TiB_2 particles were more likely to be engulfed or serve as heterogeneous sites while nano-sized TiB_2 particles would be repulsed to the solid/liquid interface to physically restrict the growth of α-Al dendrites. The strength-ductility trade-off dilemma was broken therefore superior mechanical properties were obtained in the composites. This work provides a novel perspective for manipulating Al–Si-based alloys in terms of avoiding poisoning and achieving microstructural refinement and outstanding strength-ductility synergy.

1. Introduction

Ceramic particulate reinforced aluminum matrix composites (CPRAMCs) beneficially combine the advantages of both soft aluminum matrix and stiff ceramic reinforcing phases, which endow them great capability to stretch the performance limit of traditional metallic materials and to broaden application prospects as structural components in automotive applications in recent years [1–4]. Interestingly, certain amount of ceramic particles with specific spatial distribution in the Al matrix are believed to dynamically manipulate the nucleation and growth process, thereby tailoring a homogeneous and refined composite microstructure [2,5–7]. Nevertheless, a longstanding challenge of the trade-off relationship between strength and ductility still encounters a bottleneck to the practical applications of CPRAMCs and has not been effectively overcome till now [7–9]. Moreover, Al–Si-based series alloys perform a set of superior characteristics, including high strength-to-weight ratio, cost-effective formability, excellent corrosion resistance and wear resistance. However, in the aluminum alloys with high Si contents (>3%), ceramic particles display poor chemical stability and wettability, which may result in the formation of poisonous phases and significantly impair the tailoring capacity of ceramic particles [10–13]. To overcome these intractable issues, an appropriate and meticulous ceramic particle design, synthesis and incorporation strategy is definitely required for the manipulation of Al–Si alloys to obtain high performance in CPRAMCs. More importantly, the manipulation mechanism of Al–Si-based alloys by ceramic particles in terms of the size and

* Corresponding author. State Key Laboratory of Automotive Simulation and Control, Jilin University, PR China.
E-mail address: yanghy@just.edu.cn (H.-Y. Yang).

https://doi.org/10.1016/j.compositesb.2021.108912
Received 23 February 2021; Received in revised form 3 April 2021; Accepted 13 April 2021
Available online 17 April 2021

morphology of the ceramic particles and the characteristics of the particles/matrix interfaces should also be sound understood to achieve tailored microstructures and enhanced strength-ductility synergy in Al–Si-based alloys [12,14,15].

Among well-known reinforcements, TiB_2, which performs high specific strength, extremely high hardness, high melting point and low thermal expansion coefficient, is regarded as an outstanding reinforcement in metal matrix composites [16–20]. However, TiB_2 particles synthesized by conventional methods are generally in submicron/micron size and with hexagonal plate-like morphologies, which may cause local stress concentrations and degrade their reinforcing effects [21,22]. Even worse, the incorporation and manipulation processes of those TiB_2 particles are usually accompanied by the formation of the unavoidable Al_3Ti intermediate phase [23–26]. This intermediate phase is thermodynamically prone to react with Si atoms, thereby forming Ti_5Si_3 layers on TiB_2 particles [10,13]; this immensely reduces the heterogeneous nucleation rate of α-Al and deteriorates the final mechanical performance of the matrix. However, different from the silicide coat poisoning theory, recently, Li et al. [11,12] have demonstrated that the segregation of Si atoms at the TiB_2/α-Al interface would cause Si poisoning. The formation of Ti–Si covalent bond within $TiAl_3$ two-dimensional compound (critical for triggering the nucleation of α-Al on TiB_2) can obstruct the α-Al epitaxial nucleation and hence lead to Si poisoning. As such, some Ti-free or low-Ti content master alloys that contain B-terminated TiB_2 or AlB_2 particles were designed recently for Al–Si-based alloys [27]. Nevertheless, researchers revealed that both the B-terminated TiB_2/α-Al interface and the Al_3Ti/α-Al interface are less stable than the Ti-terminated TiB_2/α-Al interface according to density functional theory calculations [28,29]. More importantly, Ti-terminated TiB_2 is more favorable for α-Al grain refinement compared to B-terminated TiB_2 and Al_3Ti [30,31]. These results reveal that developing Ti-terminated TiB_2 particles with almost no Al_3Ti phase is of great significance for effective manipulation of Al–Si-based alloys, yet this still needs a suitable synthesis strategy in the current research stage.

Compared to the type of reinforcement, the characteristics of particles/matrix interface play a more significant role in tuning the microstructures and mechanical properties of a composite when the reinforcing particles are refined to nanoscale [32,33]. Specifically, by manipulating their spatial distribution, the nanoparticles can induce microstructural evolution of the matrix during solidification process [13,32–36]. Recently, Guo et al. [35] reported that nanoparticles distributed around the growing solid-liquid interface can alter the α-Mg dendritic morphology. Cao et al. [36] suggested that nanoparticles pushed to the grain boundaries owing to the slow cooling rate can physically restrict the growth of Cu grains. As for the Al-based matrix, Chen et al. [32] found that nanoparticles could be assembled at the phase/matrix interface, which hindered the solute transport and suppressed the further growth of Bi-rich droplets in Al–Bi-based composites. Wang et al. [13,33] further reported remarkable performance enhancement in *C*P-Al and Al–10Si alloys through tailoring the distribution (i.e. intragranular and intergranular distribution) of $TiC_{0.5}N_{0.5}$ nanoparticles in the matrix. Most recently, Zan et al. [37] revealed that Al_2O_3 particles distributed at grain boundaries were more favorable to enhance high-temperature strength of the Al metal matrix composites by strengthening grain boundaries and hindering dislocation annihilation compared to intragranular Al_2O_3 nanoparticles. Therefore, owing to the manipulation of the specific spatial distribution of nanoparticles in the matrix during the grain growth, reinforcing nanoparticles exhibited superior strengthening effects compared with micron-scale particles for enhancing strength-ductility synergy [8,9]. By contrast, according to the free-growth model, large-sized particles exhibited prominent heterogeneous nucleation capacity than nanoparticles, owing to lower nucleation undercooling [24]. Besides, according to our previous researches, compared with the particles with sharp edges and corners, near-spherical particles were more effective to manipulate the mechanical performance of composites by preventing stress concentration, thereby exhibiting better compressive mechanical performance [38,39]. Therefore, during the processes of heterogeneous nucleation and grain growth, there exists a complementary relationship between submicron/micron-sized particles and nanoparticles with desirable morphologies, which stimulates better strengthening effects. In our previous work, we had found that the hybrid-sized TiC or TiC–TiB_2 ceramic particles exerted excellent manipulating capacity in enhancing strength-ductility synergy of Al–Cu-based composites [40,41]. However, the instability of TiC in Al–Si-based alloys may plague their strengthening effects, and thereby a proper strategy for targeted design and controllable synthesis of size- and morphology-tunable in-situ TiB_2 particles should be investigated for the manipulation of Al–Si-based alloys. This strategy can help optimize the spatial distribution of those particles in the matrix and synergistically deliver balanced mechanical performance of composites.

As such, this work proposed an in-situ synthesis strategy by combustion synthesis in Al–Ti–B reaction system to elaborately tune the size, morphology and crystallographic terminated planes of TiB_2 particles in TiB_2/Al precursors. Furthermore, the size-tunable TiB_2 particles released from TiB_2/Al precursors were therefore delivered into Al–Si alloys to construct TiB_2 particles reinforced Al–Si-based composites. By manipulating the spatial distribution of the nano-, submicron- and micron-scale TiB_2 particles in the Al–Si-based alloys with better particles/matrix interface performances, the microstructure could be tuned and strength-ductility synergy was also enhanced in size-tunable TiB_2 particles reinforced the Al–Si-based composites.

2. Materials and experiments

In this work, TiB_2 particles from TiB_2/Al precursors with different sizes and morphologies were fabricated by combustion synthesis from Al (99.0 wt% purity and ~28 μm in size), Ti (99.5 wt%, ~30 μm) and B (99.0 wt%, ~0.5 μm) powders. The influences of different theoretical TiB_2 contents and the molar ratio of B/Ti, as shown in Table 1, on the size and morphology of TiB_2 in each sample were investigated.

As shown in Fig. 1, the samples were synthesized by the following steps. The reactants were uniformly mixed by mechanical milling with ZrO_2 milling balls for 20 h at 50 rpm. The mixtures were cold-pressed into Φ30 × 40 mm cylinders (with relative density of 65–75%) under an axial force of 70 kN and then placed in a vacuum sintering furnace to induce the combustion synthesis reaction in the Al–Ti–B system. The heating rate in the furnace was approximately 30 °C/min, and the vacuum was lower than 50 Pa. During heating, after a sharp change in temperature detected by a W5-Re26 thermocouple, which corresponded to the formation of TiB_2 particles with a large amount of heat release, the heating was stopped, and the final product was cooled to room

Table 1
Reactants compositions in each sample of the Al–Ti–B system.

Factor	Samples	Reactants composition		Theoretical final TiB_2 content (wt%)
		Ti: B (at. %)	Ti: B (wt %)	
TiB_2 content	10-B/Ti-2.0	1 : 2.0	2.2 : 1	10
	20-B/Ti-2.0	1 : 2.0	2.2 : 1	20
	30-B/Ti-2.0	1 : 2.0	2.2 : 1	30
B/Ti molar ratio	20-B/Ti-2.4	1 : 2.4	1.9 : 1	20
	20-B/Ti-3.2	1 : 3.2	1.4 : 1	20
	20-B/Ti-4.0	1 : 4.0	1.1 : 1	20
Comparison	50-B/Ti-2.4	1 : 2.4	1.9 : 1	50

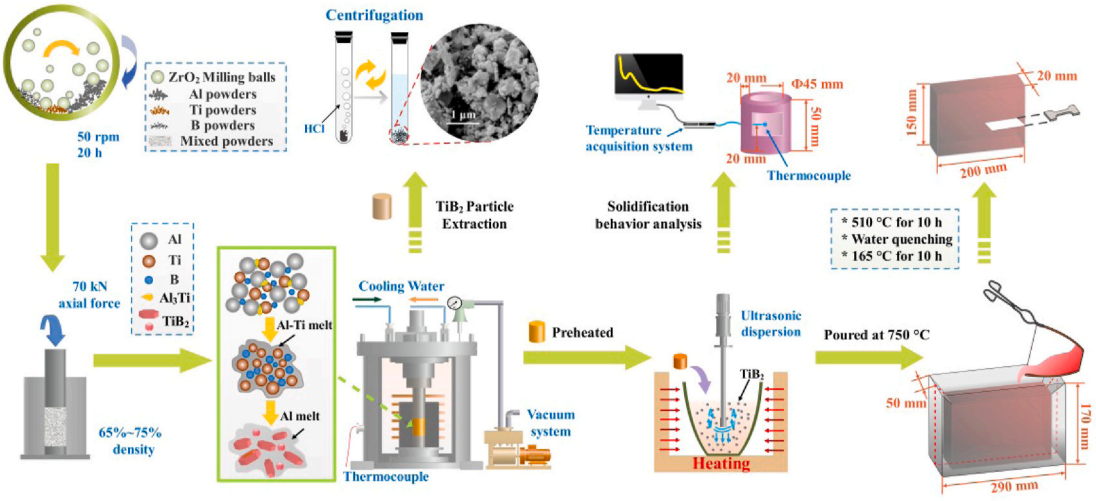

Fig. 1. Schematic illustration of the reaction processes, including fabrication of TiB_2/Al precursors and manipulation of microstructures and mechanical properties for TiB_2 reinforced Al–Si-based composites.

temperature under vacuum in the furnace. A 15–30 vol% HCl aqueous solution was adopted for the dissolution of the Al matrix to reveal the three-dimensional (3D) morphologies of the as-synthesized TiB_2 particles. More details of the sample preparation were described in Ref. [3].

Then, the grain refinement ability of size-tunable TiB_2 particles was performed in the matrix of hypoeutectic Al–Si alloy (Al-7.1Si-3.8Cu-0.1Fe-0.1Mn, wt%). First, the as-synthesized TiB_2 particles in 20-B/Ti-2.4 and 50-B/Ti-2.4 systems were preheated to 600 °C and held isothermally for at least 1 h before being fed into the Al–Si melt. The Al–Si alloy was melted in a resistance furnace in advance. The previously mentioned TiB_2/Al precursors were added into the melt at 850 °C and then stirred sufficiently for 3 min by a graphite rod. Here, ultrasonic treatment was utilized to further disperse the TiB_2 particles in the Al–Si melt. An ultrasonic niobium probe was preheated and immersed into the Al–Si melt for about 20 mm and ultrasonically treated at 750 °C under a frequency of 19.9 kHz for 5 min. Finally, the melt with dispersed TiB_2 particles was poured into a preheated steel permanent mold (with dimension of 290 mm in length, 50 mm in half-width and 170 mm in height) at 750 °C, and the as-fabricated cast was in the dimension of 200 × 20 × 150 mm^3. A reference sample free of TiB_2 particles was also fabricated in the same condition, and this reference was named UM hereafter. Also, Al–Si-based composites manipulated by 50 wt% TiB_2/Al precursor and 20 wt% TiB_2/Al precursor were synthesized in 50-B/Ti-2.4 sample and 20-B/Ti-2.4 sample respectively and they were named as MM and MN respectively hereafter. The heat treatments of the alloys in this work were performed before tensile testing. First, all as-cast samples were kept at 510 °C for 10 h followed by water quenching. Second, all quenched samples were aging-treated at 165 °C for 10 h followed by air cooling.

During cooling, the solidification behavior with different types of TiB_2 particles was detected by a K-type thermocouple connected to a data-logger system. The melts with or without the TiB_2/Al precursors were respectively cast into a cylindrical refractory brick mold (Φ45 mm × 50 mm, thickness 20 mm) with a cooling rate of 0.8 °C/s at the center of the mold (20 mm above the bottom) to detect the corresponding cooling curve. The thermal data analysis were carried out in terms of the Al–Si solidification characteristic analysis in Ref. [42], in which some characteristic temperatures were defined as T_{nuc}, $T_{\min}$ and T_g, corresponding to the primary phase nucleation, unsteady-state growth and steady temperature, respectively. Accordingly, ΔT_{Rec} was the recalescence undercooling between the unsteady temperature and the steady growth temperature; that is, $\Delta T_{Rec} = T_{\min} - T_g$.

Phase identifications of the as-synthesized master alloys were conducted using an X-ray diffractometer (XRD, D/Max 2500 PC Rigaku, Japan) with Cu-K_α radiation, a scanning speed of 4°/min and a scanning range of 20°–80°. The size distributions and 3D morphologies of the TiB_2 particles were characterized by field emission scanning electron microscopy (FESEM, JSM 6700F, Japan). The as-cast Al–Si-based alloys before and after manipulating by size- and morphology-tunable TiB_2 particles were mechanically ground, polished and etched by 5 vol% HBF_4 solution. Then, the microstructures were characterized by optical microscopy (OM, Olympus PMG3, Japan) and scanning electron microscopy (SEM, Tescan vega3 XM, Czech Republic). The Al/TiB_2 interface and the θ' phase were observed by high-resolution transmission electron microscopy (HRTEM, JEM-2100F, Japan). Tensile tests of the heat-treated samples which had cross-sectional dimensions of 4.0 × 2.5 mm^2 and a gauge length of 10.0 mm were performed by a servo-hydraulic material testing equipment (MTS 810, USA).

3. Results and discussions

3.1. Size and morphology manipulation of the TiB_2 particles in the Al–Ti–B system

It is known that, during the heating process of combustion synthesis in the Al–Ti–B system, Ti particles can easily start to react with Al at a relatively low temperature (around the Al melting point) to form Al_3Ti through the following reaction in Eq. (1).

$$3Al(L) + Ti(S) = Al_3Ti(S) \quad (1)$$

$$\Delta G_1 = -154.904 + 4.205 \times 10^{-2}T \text{ (kJ/mol)}$$

Accompanied by a large amount of heat release during this reaction, Al_3Ti is synthesized first and then partly dissolves to form Al–Ti melt. The reaction between Al and Ti also provides sufficient energy for the subsequent formation of TiB_2 particles between B atoms and Ti atoms. Under a higher temperature condition, B also dissolves into the Al–Ti melt. When a critical concentration of B in the liquid phase is achieved, TiB_2 particles are expected to form under the reaction Eq. (2) with higher kinetics. It is also suggested that TiB_2 is more stable than Al_3Ti in this Al–Ti–B system, and the transformation of Al_3Ti and B into TiB_2 is feasible from the viewpoint of thermodynamics.

$$Al_3Ti(S) + 2B(S) = TiB_2(S) + 3Al(L) \quad (2)$$

$$\Delta G_2 = -186.085 - 1.128 \times 10^{-2}T \text{ (kJ/mol)}$$

Fig. 2(a) shows the phase constitution of the 10 wt%TiB_2/Al, 20 wt%

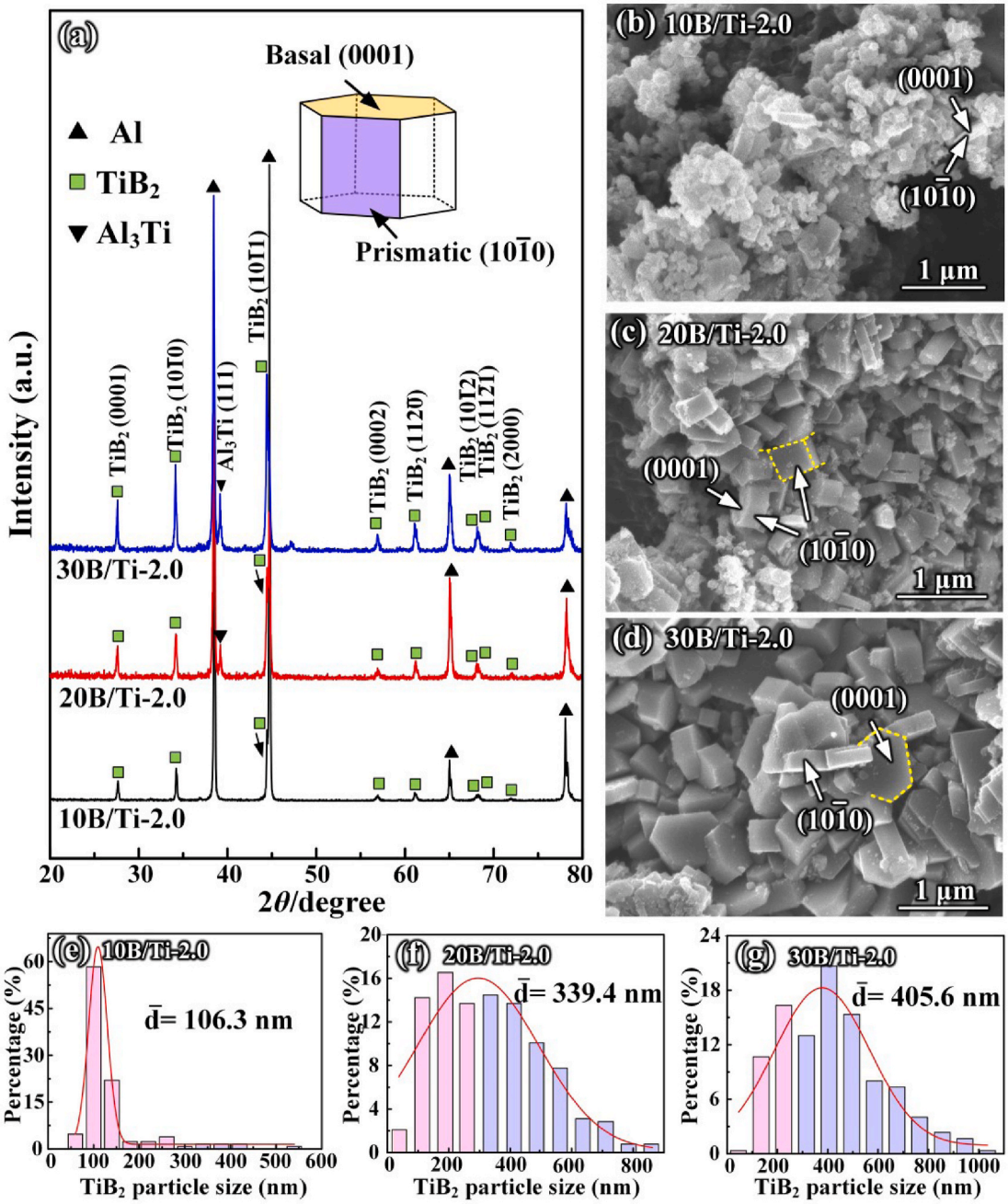

Fig. 2. (a) XRD patterns, (b–d) SEM morphology and (e–g) corresponding size distribution of TiB_2 particles for the TiB_2/Al matrix composites with different TiB_2 contents.

TiB_2/Al and 30 wt%TiB_2/Al precursors synthesized from the 10-B/Ti-2.0, 20-B/Ti-2.0 and 30-B/Ti-2.0 samples. The α-Al, TiB_2 and Al_3Ti phases can be detected at this B/Ti molar ratio (=2). An Al_3Ti diffraction peak is detected in these samples, which suggests that the transformation of Al_3Ti and B into TiB_2 is incomplete. Actually, due to the high heating rate and the instantaneous ignition process, the reactions between Al, Ti and B during the combustion synthesis are far from equilibrium, which makes the solute atoms non-uniformly distribute and finally remain as Al_3Ti phase [43].

The size distribution and 3D morphology of these as-extracted TiB_2 particles from the precursors are shown in Fig. 2(b–d). Here, typical hexagonal plate-like TiB_2 with basal (0001) and prismatic (10$\bar{1}$0) planes can be seen in each sample. As the theoretical TiB_2 content increases from 10 to 30 wt%, the average size of the TiB_2 particles (Fig. 2(e–g)) significantly increases from ~106 nm to ~406 nm, and most curved edges disappear. The coarsening of TiB_2 particles is attributed to the increase in combustion temperature with the decrease of Al content.

Further increasing the B/Ti ratio while maintaining the same 20 wt% TiB_2 significantly reduces the fraction of Al_3Ti phase in the composites, as shown in Fig. 3(a). The Al_3Ti phase is even exhausted and AlB_{12} phase is present in the 20-B/Ti-3.2 and 20-B/Ti-4.0 samples. As seen from Fig. 3(b–d), with increasing the B/Ti molar ratio, some high-index crystal planes, i.e. chamfered (1$\bar{2}$12) and prismatic (11$\bar{2}$0) planes are observed, and most particles display a polyhedral or near-spherical morphology in the sample of 20-B/Ti-4.0. The size distributions (Fig. 3(e–g)) also suggest that the average particle size decreases as increasing the B content from ~339 nm in 20-B/Ti-2.0 to ~205 nm in 20-B/Ti-4.0, and the size distribution becomes more uniform. It is

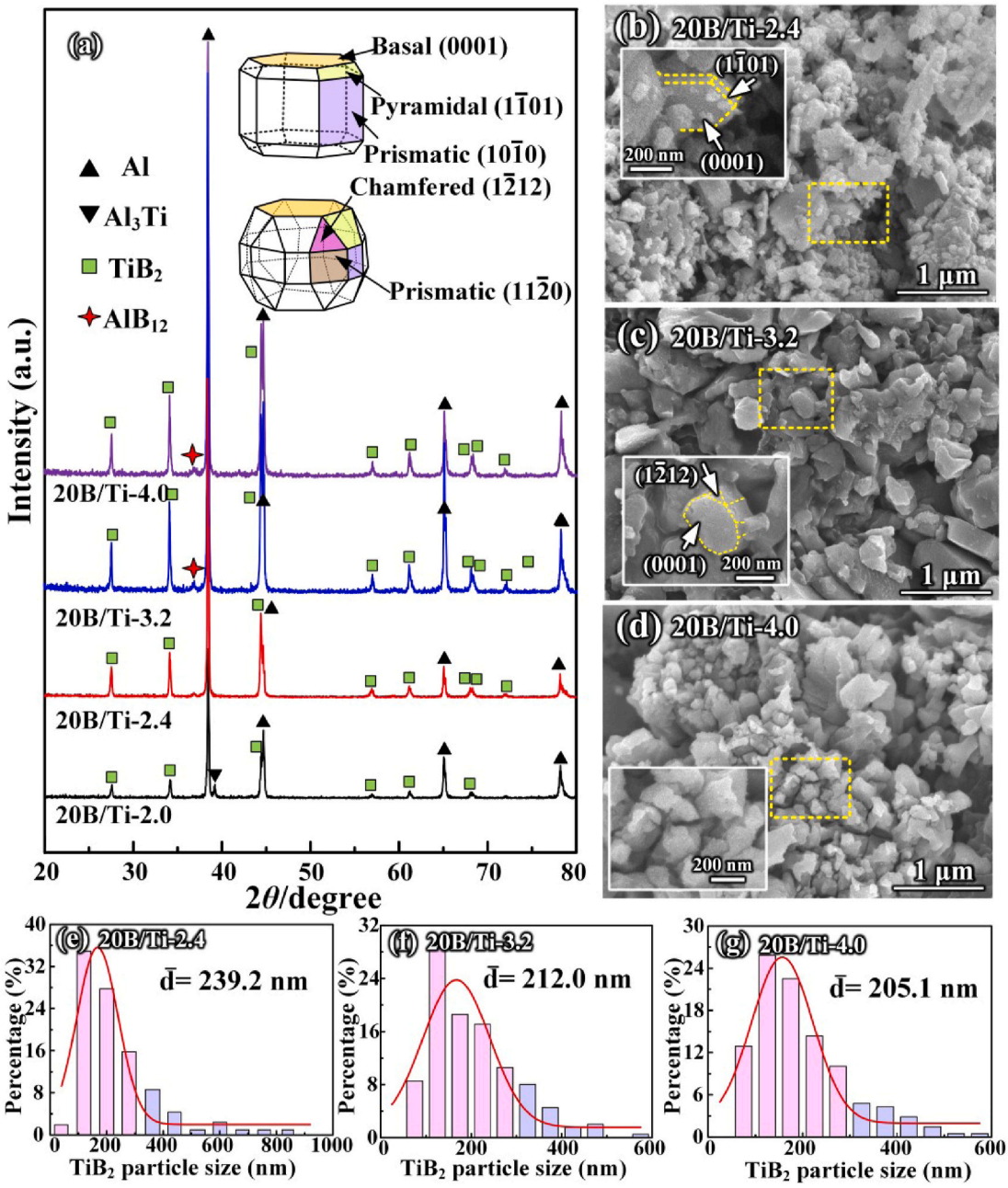

Fig. 3. (a) XRD patterns of 20 wt% TiB_2/Al precursors with different B/Ti molar ratios. Morphology of the TiB_2 particles extracted from the (b) 20-B/Ti-2.4, (c) 20-B/Ti-3.2 and (d) 20-B/Ti-4.0 synthesis systems. (e–g) size distribution of the TiB_2 particles from different synthesis systems.

known that the increase in B concentration during the reaction in the Al–Ti liquid would promote the ignition process, i.e. the reaction of Al_3Ti and B into TiB_2, as the ignition process becomes easier and starts at a lower temperature [44]. Nevertheless, the excessive B atoms in the reaction system would absorb on the α-Al/TiB_2 interface, which induces irregular growth of the basal (0001) and prismatic (10$\bar{1}$0) planes. Other high-index planes are thus observed, and TiB_2 particles transform into fine and irregular polyhedrons or near-spheres.

Moreover, Wang et al. [22] suggested that the surface energy of TiB_2 low-index planes is related to the chemical potential of Ti or B. Under the Ti-rich condition, the stability of TiB_2 low-index surface structures in Fig. 4(a) follows the following sequence: (0001) or (10$\bar{1}$0) Ti-terminated > (11$\bar{2}$0) > (0001) B-terminated > (10$\bar{1}$0) B-terminated. Fig. 4(b) illustrates the most stable hexagonal close-packed (HCP) bonding structure calculated by Han [28] or Deng [21] concerning the Al/TiB_2 interface. The (0001) Ti-terminated interface has a higher work function than the (0001) B-terminated interface because of the higher bonding energy of Al–Ti than of Al–B. As illustrated in Fig. 4(b), the Ti-terminated TiB_2/Al interface is more stable at a lower B chemical potential, whereas a higher B chemical potential in the reaction system is favorable for the stability of the B-terminated TiB_2/Al interface. Therefore, the atomic concentration in the melt indeed influences the Al/TiB_2 interface system therefore the morphology evolution of TiB_2 particle in the Al melt. Moreover, it was reported that Ti-terminated TiB_2 could induce five ordered Al layers, whereas B-terminated TiB_2 could only induce one Al layer on the TiB_2 substrate [29], which also suggests that different terminate interfaces may exert distinct nucleation effects. For the samples of 20-B/Ti-2.0, 20-B/Ti-2.4 and 20-B/Ti-3.2 in this work, TiB_2 is still Ti-terminated. When further increasing the B concentration to B/Ti = 4, which means that the weight ratio between Ti

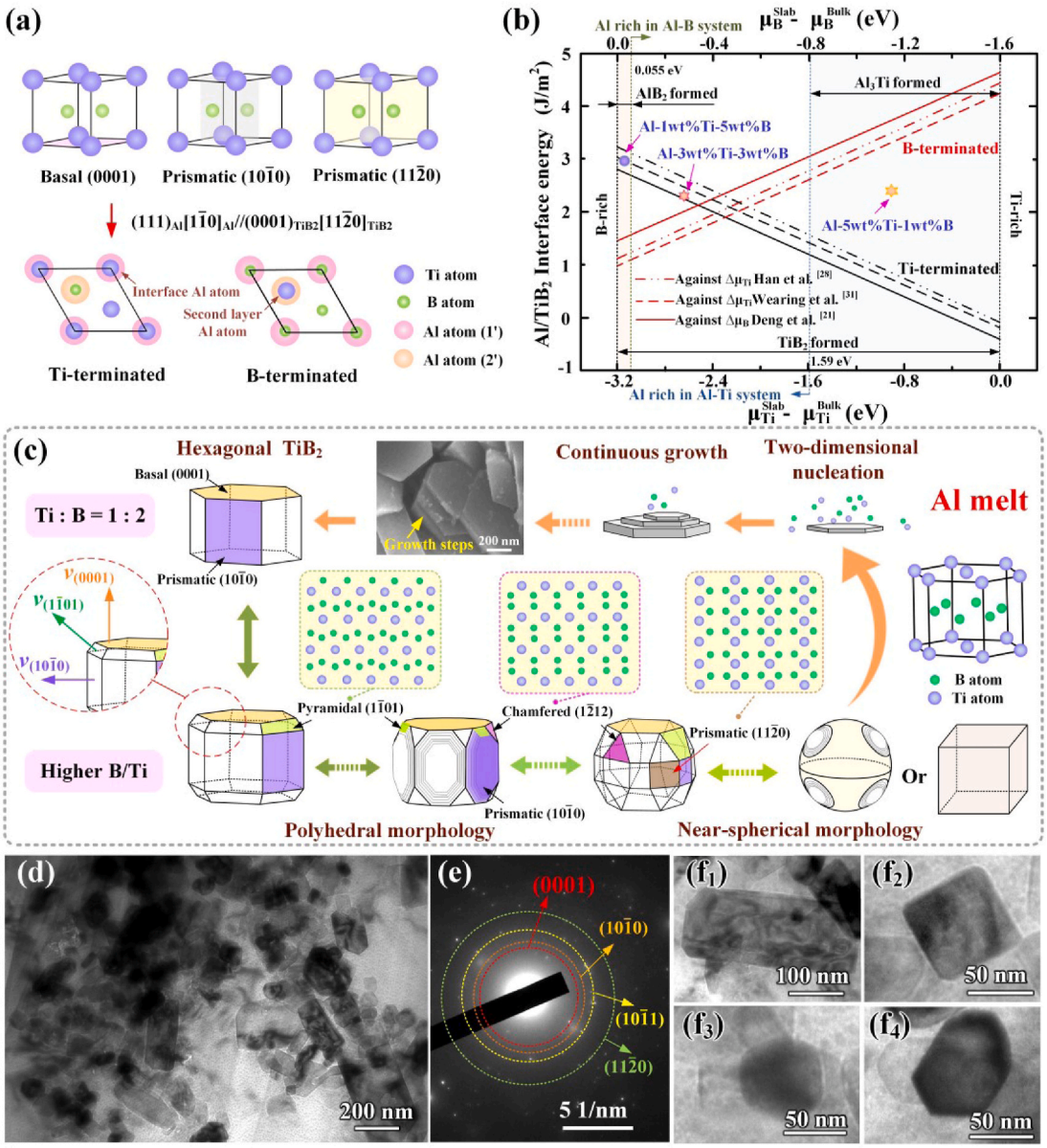

Fig. 4. (a) Three low-index surface structures of TiB_2 and HCP stacking sequences of the $(111)_{Al}/(0001)_{TiB2}$ interface. (b) Interfacial energies of Ti- and B-termination Al/TiB_2 interfaces and some samples of Al-5wt%Ti-1wt%B, Al-3wt%Ti-3wt%B and A-1wt%Ti-3wt%B master alloys based on B chemical potential. (c) The mechanism for nucleation and growth evolution of TiB_2 nanoparticles under the influence of B/Ti molar ratio. (d) TEM morphology of the 20 wt% TiB_2/Al precursors synthesized in the 20-B/Ti-2.4 system and (e) the corresponding SAED pattern; (f) The high magnification TEM image of the particles with different morphologies.

and B approaches Al-3wt%Ti-3wt%B, Ti-terminated TiB_2 gradually transforms into B-terminated TiB_2. The corresponding TiB_2 nanoparticles morphology evolution mechanism is illustrated in Fig. 4(c). For a high Jackson alpha-factor, TiB_2 exhibits a two-dimensional (2D) nucleation growth model [45,46]. The 2D nucleus seems to be enclosed by the relatively stable edges and planes such as (0001) and (10$\bar{1}$0) because the creation of 2D nucleus edges is an energy-consuming process, and the low-index (0001) and (10$\bar{1}$0) planes have the lowest interfacial energy in the Al melt. Then, after a thin hexagonal nucleus is formed, the surrounding B and Ti atoms would deposit rapidly on the platelets. However, the 2D nucleation rate is higher than the atom spreading rate on the newly formed platelets, which leads to the stepped growth between the adjacent platelets in Fig. 4(c). During these nucleation and growth processes, TiB_2 particles grow into perfect hexagonal prisms under normal growth conditions, whereas the variation of B concentration would launch the morphology evolution of those particles. The addition of B atoms almost refines the particles by the absorption on the specific planes and reduces the growth ratio of the corresponding plane. Therefore, some high-index planes are formed, most sharp edges and corners disappear, and the hexagons are thus transformed into polyhedrons or near-spheres with curved edges. The TEM image shown in Fig. 4(d) illustrates the morphologies of the 20 wt % TiB_2/Al precursors synthesized in 20-B/Ti-2.4 reaction system, and the selected area electron diffraction (SAED) pattern in Fig. 4(e) demonstrates that the exposed planes of in-situ TiB_2 particles in the Al matrix are mainly (0001), (10$\bar{1}$0), (11$\bar{2}$0) and (10$\bar{1}$1). Interestingly, the TiB_2 particles with the morphology of typical hexagon, cube, polyhedron or near sphere with curved edges are also observed in Fig. 4(f). This suggests that the particle morphology can be successfully tuned by the design and controllable synthesis in Al–Ti–B systems.

3.2. Fabrication of high-performance TiB_2 reinforced Al–Si-based composites

3.2.1. Interface crystallographic matching

It is known that a good crystallographic matching between the reinforcement and the matrix at the interface has low interfacial energy, thereby facilitating heterogeneous nucleation and grain refinement. As such, the manipulation of TiB_2 reinforced Al–Si-based composites significantly relies on good interfacial bonding between the reinforcement particles and the Al–Si alloy matrix. Fig. 5 (a) shows the crystallographic orientation relationships (ORs) of α-Al/TiB_2 and Si/TiB_2 interfaces determined by the edge-to-edge model (E2EM) with respect to the crystal structures and possible exposed planes of Al, Si and TiB_2.

The interatomic spacing mismatch f_r along with the possible matching directions and the interplanar spacing mismatch f_d between close or nearly close-packed planes of TiB_2 with Al and Si matrix can be defined as the following Eqs. (3) and (4), and an OR is considered to exist when the values of f_r and f_d are equal or less than the critical value of 10% [47–49].

$$f_r = \left|\frac{r_M - r_P}{r_P}\right| \tag{3}$$

$$f_d = \left|\frac{d_M - d_P}{d_P}\right| \tag{4}$$

where r_M and r_P are the interatomic spacings along a certain close-packed (CP) row of the Al or Si matrix and TiB_2, respectively, and d_M and d_P are the interatomic spacings between certain CP planes or possible exposed crystal planes of the Al or Si matrix and TiB_2, respectively. Considering that the construction of matching rows should lie in the matching planes, the possible ORs between α-Al/TiB_2 and Si/TiB_2 with a relative lower f_d and f_r are presented in Table 2, which suggests

Table 2
The crystallographic orientation relationships (ORs) and the corresponding interplanar spacing mismatch (f_d) and interatomic spacing mismatch (f_r) between Al/TiB_2 and Si/TiB_2.

ORs	Matching planes	f_d	Matching rows	f_r
Al/TiB_2	$\{200\}_{Al}//\{10\bar{1}1\}_{TiB2}$	0.54%	$<110>_{Al}//<11\bar{2}0>_{TiB2}$	5.45%
	$\{220\}_{Al}//\{11\bar{2}0\}_{TiB2}$	5.48%	$<112>_{Al}//<10\bar{1}0>_{TiB2}$	5.47%
Si/TiB_2	$\{111\}_{Si}//\{0001\}_{TiB2}$	2.84%	$<112>_{Si}//<11\bar{2}0>_{TiB2}$	9.80%
	$\{111\}_{Si}//\{11\bar{2}0\}_{TiB2}$	3.69%	$<112>_{Si}//<0001>_{TiB2}$	3.23%

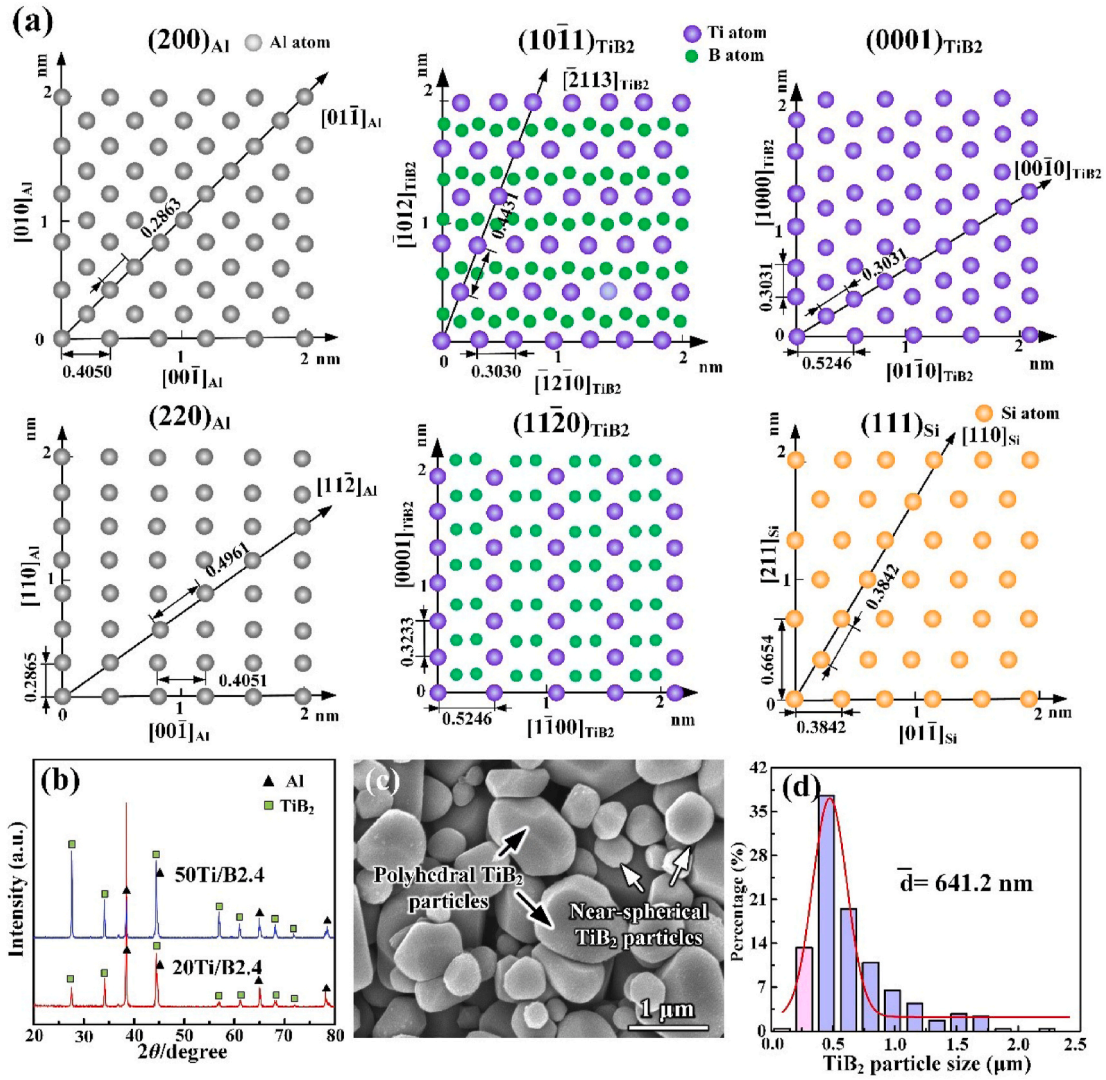

Fig. 5. (a) Atomic configurations on the corresponding CP or exposed crystal planes of Al, Si and TiB_2. (b) XRD patterns of 20 wt% TiB_2/Al precursors and 50 wt% TiB_2/Al precursors synthesized by 20-B/Ti-2.4 and 50-B/Ti-2.4 systems. (c) FESEM image and (d) size distribution of the as-extracted TiB_2 particles synthesized in the 50-B/Ti-2.4 system.

that TiB_2 particles can be excellent nucleation sites for α-Al and Si with the exposure of {0001}, {10$\bar{1}$1} and {11$\bar{2}$0} crystal planes.

As known, the size, morphology and terminated atoms of the TiB_2 particles and the residual intermediate phase in TiB_2/Al precursors strongly affect their manipulation effects in the Al matrix, especially the Al–Si matrix. In the 20-B/Ti-2.4 sample, such B concentration is favorable to reduce the Al_3Ti intermediate phase in order to avoid Ti–Si poisoning, and the as-synthesized TiB_2 particles are still Ti-terminated with submicron-/nano-scale and spherical or hexagonal morphology. As such, well-designed TiB_2 particles fabricated in the 20-B/Ti-2.4 system were specially selected to manipulate hypoeutectic Al–Si alloy to construct TiB_2 reinforced Al–Si-based composites. Additionally, micro-sized TiB_2 particles fabricated in a 50-B/Ti-2.4 system are also incorporated with the same content level of 0.7 wt% to verify the size effects, i.e., microscale and nanoscale, on the manipulation of TiB_2/Al–Si-based composites during the heterogeneous nucleation and free growth processes. As shown in Fig. 5(b), no Al_3Ti could be detected in the 20-B/Ti-2.4 or 50-B/Ti-2.4 systems. For particles synthesized from 50-B/Ti-2.4 systems, these TiB_2 particles display polyhedral or near-spherical morphologies almost in the submicron/micron-scale (Fig. 5(c and d)).

3.2.2. *Microstructures manipulation of TiB_2 reinforced Al–Si-based composites*

To verify the size effects (nano-sized, submicron- and micro-sized) of reinforcing particles on the manipulation of microstructures and performances of Al–Si composites, TiB_2 reinforced Al–Si-based matrix composites are constructed by incorporating size-tunable TiB_2 particles. As seen from Fig. 6(a–c), α-Al dendrites transform from coarse dendrites to fine equiaxed structures in the MN sample, whereas some columnar dendrites are still observed in the MM sample. The average sizes of the α-Al grain in the MM and MN samples are ~506 μm and ~237 μm, respectively, which are refined by 55.5% and 79.2%, respectively, compared with the average size of the α-Al grain in un-manipulated matrix alloy (~1138 μm). Interestingly, the typical eutectic Si microstructures are altered by manipulating the micron/submicron-sized and nano/submicron-sized TiB_2 particles in both the as-cast condition (Fig. 6 (d–f)) and the T6 heat treatment (Fig. 6(g–i)). In the as-cast condition, the eutectic Si displays a plate-like morphology with an average size of 18.5 μm in the UM sample, which substantially transforms to long needle-like morphology with an average size of 16.9 μm in the MM sample and to short needle-like morphology with a size of 8.9 μm in the

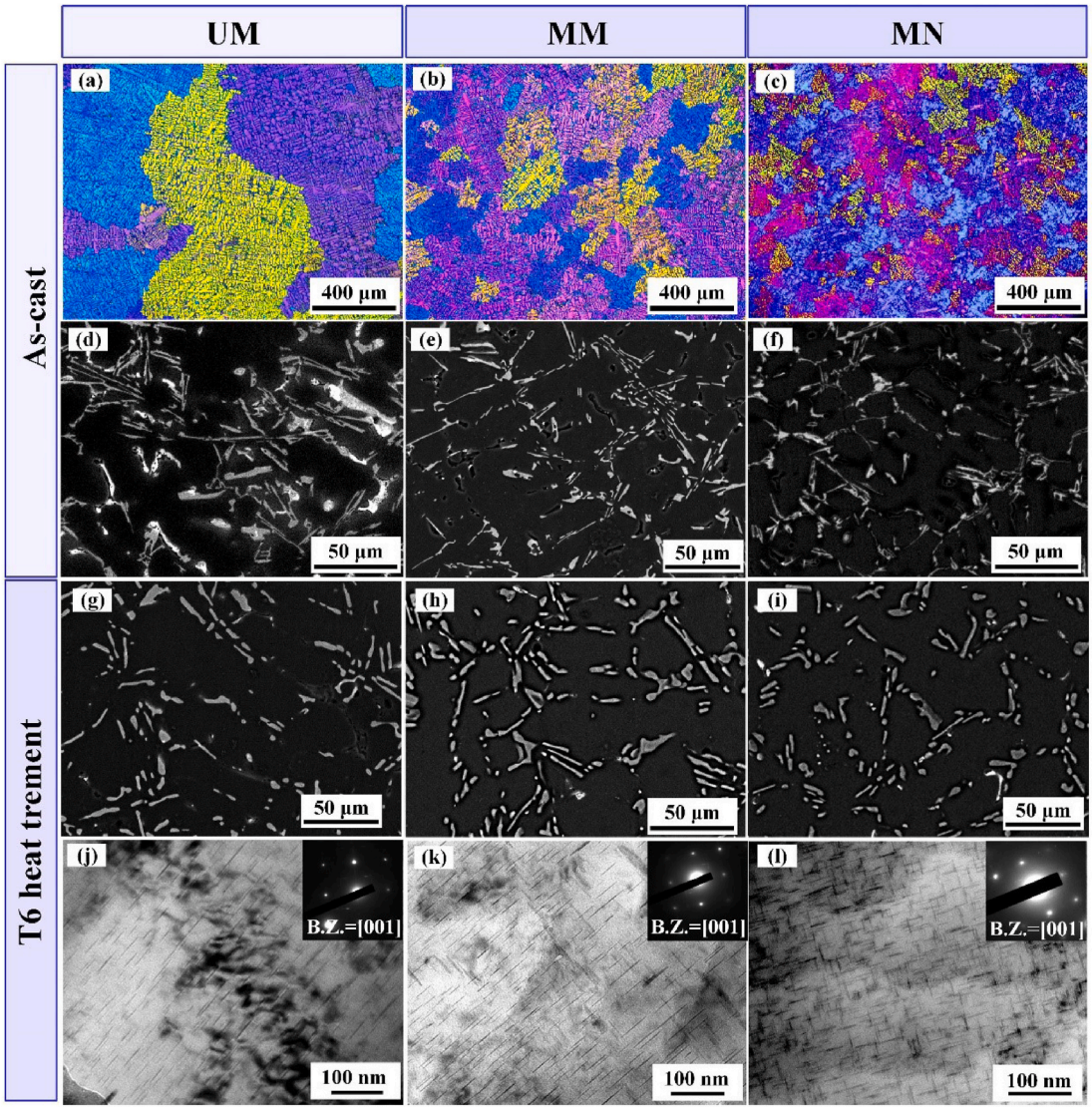

Fig. 6. Microstructure configurations in the samples of unmanipulated Al–Si based alloy (UM), TiB_2/Al–Si-based composites manipulated by micro-/submicron-sized TiB_2 particles (MM) and TiB_2/Al–Si-based composites manipulated by nano-/submicron-sized TiB_2 particles (MN): (a–c) Polarized optical micrographs of α-Al dendrites; backscattered SEM micrographs of the Al–Si eutectic microstructure of TiB_2/Al–Si-based composites (d–f) in the as-cast and (g–h) after T6 heat treatment; (j–l) TEM micrographs taken in the $[001]_{Al}$ zone axis showing the diameter and morphologies of the θ' precipitates after T6 heat treatment.

MN sample. The aspect ratio (i.e. the ratio of the length and width) also decreases from 12.89 in the UM sample to 8.51 in MM sample and 5.94 in MN samples. After the T6 heat treatment, most eutectic Si in the MM and MN samples transforms into a fine, short rod-like structure without sharp edges and corners compared with a long rod-like structure in UM sample. The eutectic Si shows an average size of 10.6 μm, 9.5 μm and 6.9 μm and with aspect ratios of 4.51, 3.16 and 2.26 in the UM, MM and MN samples, respectively. Furthermore, as seen from the TEM images shown in Fig. 6(j–l), compared to UM sample, θ' precipitates with a plate-like morphology are substantially refined in MM and MN samples. The MM and MN also have higher densities of θ' precipitates than the UM sample. The average diameters of θ' precipitates in the UM, MM and MN samples are about 47 nm, 39 nm and 29 nm, respectively. Consequently, Al–Si-based alloy demonstrates much finer microstructure configuration, in terms of α-Al dendrites, Al–Si eutectic and θ' precipitates, in the MN sample than in MM sample. This suggests that nanoparticles combined with submicron-sized particles are prone to be effective in the manipulation of Al–Si alloys.

3.2.3. Solidification behaviors analysis

Fig. 7(a) displays the cooling curves during the casting of the UM, MM and MN samples. Fig. 7(b) and Table 3 further show the corresponding characteristic thermal data of the primary α-Al and Al–Si eutectic, which are derived by the first and second derivatives of the cooling curves in Fig. 7(c–e). The critical nucleation temperatures of primary α-Al in both the MM and MN samples are increased. The critical

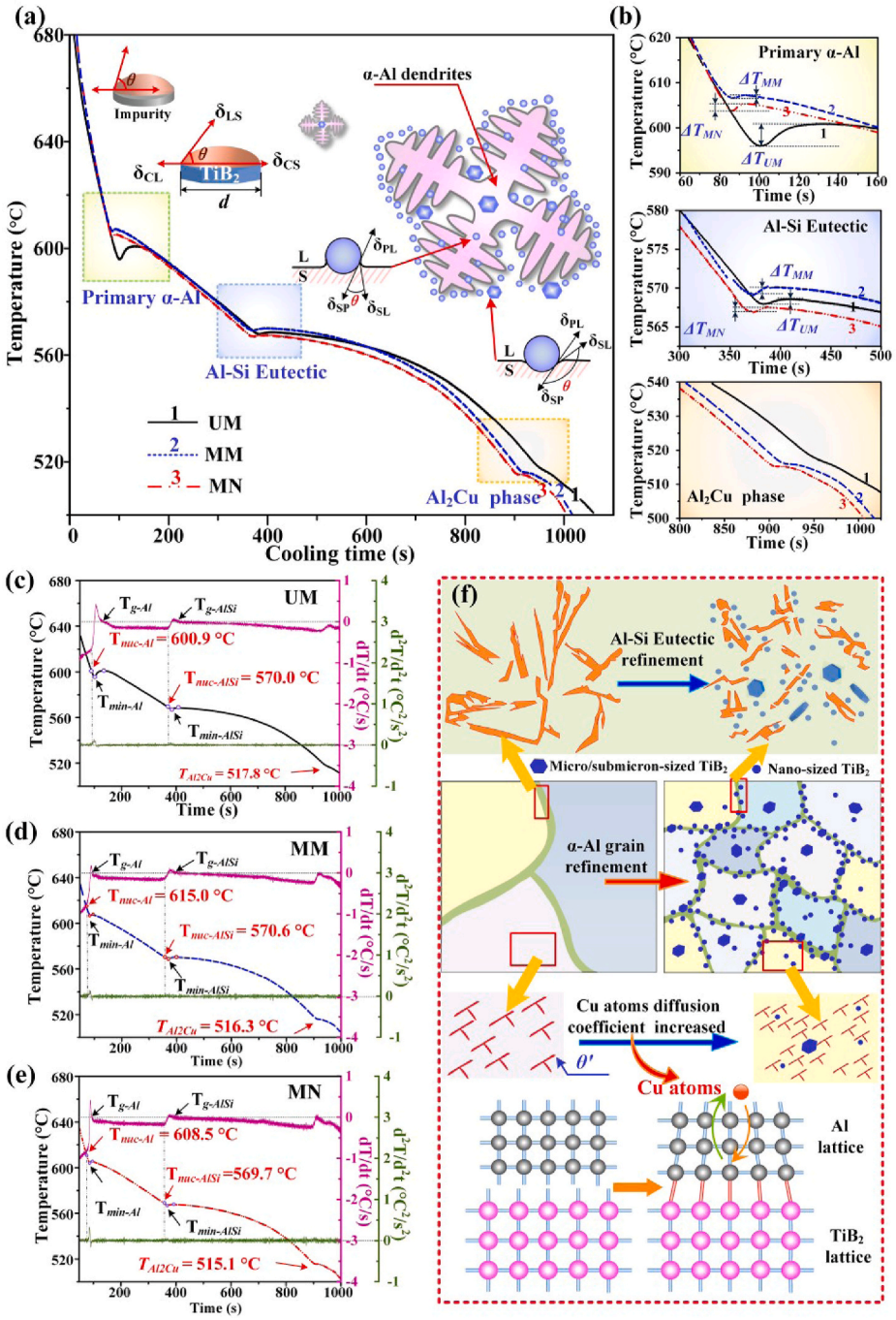

Fig. 7. (a) Cooling curves and the corresponding (b) enlarged view showing specific characteristic areas and (c–e) first and second derivatives of the cooling curve for the UM, MM and MN samples. (f) Mechanism of the evolution of primary α-Al dendrites, Al–Si eutectic and θ' precipitates by manipulating TiB_2 particles.

Table 3
Characteristic thermal analysis data of the samples of UM, MM and MN during cooling. (°C).

Samples	Manipulated reinforcement	Primary α-Al nucleation (°C)				Al–Si eutectic nucleation (°C)			
		$T_{nuc\text{-}Al}$	$T_{min\text{-}Al}$	$T_{g\text{-}Al}$	$\Delta T_{Rec\text{-}Al}$	$T_{nuc\text{-}Si}$	$T_{min\text{-}Si}$	$T_{g\text{-}Si}$	$\Delta T_{Rec\text{-}Si}$
UM	Without TiB_2 particles	600.9	595.9	600.8	4.9	570.0	567.9	598.6	0.7
MM	Micro-/submicro-TiB_2	615.0	606.6	607.2	0.8	570.6	569.3	570.1	0.8
MN	Nano-/submicro-TiB_2	608.5	603.8	605.3	1.5	569.7	567.0	567.5	0.5

nucleation temperature of primary α-Al in MM sample is about 615 °C, which is higher than the ones in the MN sample (about 609 °C) and in the UM sample (about 601 °C). The addition of micro-/submicron-scale TiB_2 particles could reduce ΔT_{Rec} of primary α-Al from 4.9 °C to 0.8 °C while nano/submicron-sized TiB_2 particles could only reduce from 4.9 °C into 1.5 °C. Furthermore, micron/submicron-sized and nano/submicron-sized TiB_2 particles decline the formation temperature of the Al_2Cu phase. The decreased ΔT_{Rec} caused by the introduction of TiB_2 particles indicates that the formation process of Al_2Cu phase by the migration of Cu atoms completes more rapidly, and nano/submicron-sized TiB_2 particles seem to have a more evident effect on the diffusion of Cu. Additionally, the introduction of TiB_2 particles with different lattice parameters could cause lattice mismatch at the Al–TiB_2 bonding interface in atomic scale, as illustrated in Fig. 7(f). Thus, α-Al lattice distortion takes place around the interfaces. The lattice distortion of α-Al increases the diffusion coefficient of Cu atoms. As such, the Cu segregation is weakened and the precipitation of θ' precipitates is significantly triggered to occur. Therefore, finer and more dispersed θ' phases can be obtained, especially around the TiB_2 particles after T6 heat treatment.

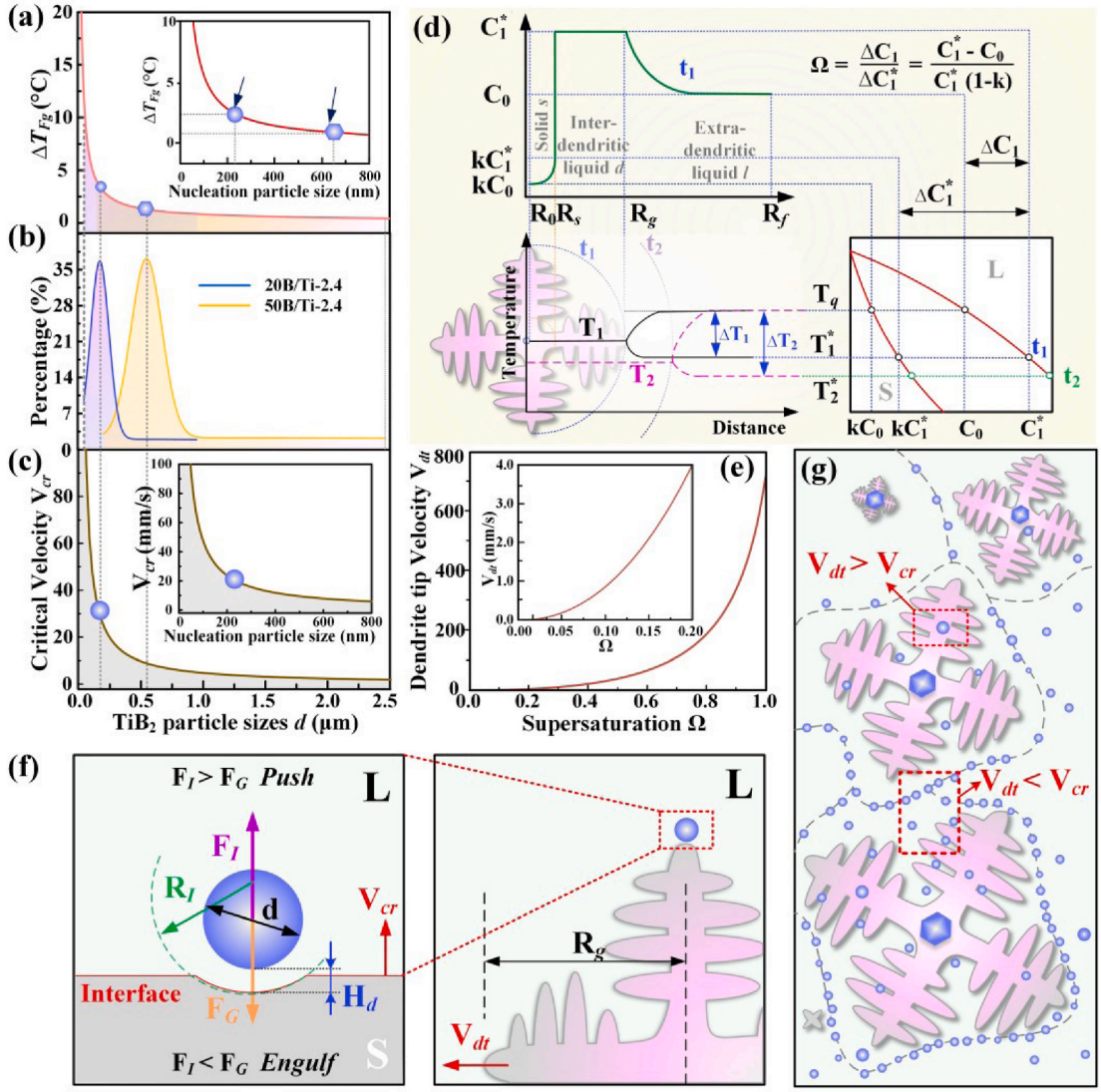

Fig. 8. (a) The relationship between the undercooling for free growth and the diameter of the nucleating particles; (b) The size distribution of micro/submicron-sized and nano/submicron-sized TiB_2 particles in 50 wt % TiB_2/Al precursor and 20 wt % TiB_2/Al precursor synthesized in 50-B/Ti-2.4 sample and 20-B/Ti-2.4 sample; (c) The highest critical interface velocities V_{cr} of α-Al. (d) A schematic representation of the solute diffusion model and constitutional supercooling region for equiaxed dendritic growth; (e) The actual dendrite tip velocity V_t of Al–Si-based alloy in this study; (f) Schematic drawing showing a particle in front of the solid/liquid interface and the actual dendrite tip growth, which details the highest critical interface velocities V_{cr} and actual dendrite tip velocity V_t.

As previously calculated, TiB_2 particles can act as effective nucleation sites for both Al and Si and further refine the α-Al grains and Si phase of the Al–Si eutectic in the TiB_2/Al–Si-based composites. By the free-growth model raised by Greer [24], the undercooling for free growth (ΔT_{fg}) and the diameter of the nucleating particles (d_0) can be simply described by Eq. (5):

$$\Delta T_{fg} = \frac{4\sigma}{\Delta S_V d_0} \tag{5}$$

where σ is the S/L interfacial energy, which is estimated by the highest available value of 0.158 J/m^2, and ΔS_V is the entropy of fusion per unit volume, which is 1.12×10^6 J/K m^3 [24]. In this work, the MM samples contain TiB_2 particles ranging from 2.5 μm to 500 nm, whereas the TiB_2 particle size in the MN sample varies from 900 nm to 50 nm. As Fig. 8(a) illustrates, the free growth undercooling of α-Al in the MM sample and in the MN sample is calculated to be 1.12–0.22 K and 11.4–0.63 K, respectively. As known, a larger nucleation substrate is more favorable for grain nucleation under a low undercooling. Therefore, smaller particles start to nucleate until this undercooling (ΔT_{Fg}) reaches their critical value. As cooling continues, the nucleated grains would grow and release latent heat. When the release of latent heat exceeds the rate of external heat extraction from casting, nucleation would stop and recalescence would start. Therefore, most nanoparticles cannot reach the critical undercooling for nucleation. However, the solidification microstructures among the UM, MM and MN samples shown in Fig. 6(a)–(c) suggest that further growth barriers are also dominant besides heterogeneous nucleation. Those nanoparticles distributed around the growing phase would sharply slow down the release rate of latent heat into the melt during the growth. This promotes the initiation of nucleation from a higher temperature under a low necessary nucleation undercooling and, in turn, enhances the nucleation efficiency. Therefore, the nucleation and growth time also decreases after the addition of micron/submicron-sized and nano/submicron-sized TiB_2 particles for both the primary α-Al and Al–Si eutectic.

It is known that nanoparticles are likely to assemble at the solid-liquid (S/L) interface during solidification, and they could be engulfed or pushed by the S/L interface in terms of the critical interface velocity V_{cr} [50], which can be described as Eqs. (6) and (7).

$$V_{cr} = \frac{\Delta\gamma_0 a_0^2}{3\eta\alpha R H_d} \frac{R_I}{R_I - R} \tag{6}$$

$$\Delta\gamma_0 = \gamma_{SP} - \gamma_{LP} - \gamma_{SL} \tag{7}$$

where γ_{SP}, $\gamma_{LP}$and $\gamma_{SL}$are the solid/particles, liquid/particles and solid/liquid interface energies, respectively; and $\Delta\gamma_0$ is calculated to be 0.4 J m^{-2} [50] and a_0 is the atomic diameter of Al, which is 2.55×10^{-10} m [51] while α is a coefficient as 0.15 according to the contact condition [52]; η is the liquid viscosity as 0.85×10^{-3} N S· m^{-2} [53]; H_d is the particle/interface separation for 1.43×10^{-8} m [54]; R_I and R are the radius of the non-planar interface (grain radius) and the average radius of the nanoparticles, respectively. When R_I » R, the value $\frac{R_I}{R_I - R}$ can be regarded as 1. The highest critical interface velocities of α-Al were calculated to be in the range of 95.1–23.7 mm/s when the particles are 50–200 nm, as illustrated in Fig. 8(b) and (c).

Generally, after heterogeneous nucleation, those existing grains begin to grow. The diffusion coefficient of those alloying elements in the Al melt follows the Arrhenius relationship in Eq. (8):

$$D = D_0 e^{-E_\alpha / k_B T} \tag{8}$$

here, D_0 is the pre-exponential factor, which is 1.34×10^{-7} m^2 s^{-1} for Si and 1.06×10^{-7} m^2 s^{-1} for Cu; E_a is the activation energy of 30 kJ/mol for Si and 24 kJ/mol for Cu [55]. k_B is the Boltzmann constant 1.38×10^{-23} J K^{-1} and T is the temperature according to the liquidus temperature of Al–7Si–4Cu. Therefore, the diffusion coefficients of Si and Cu in the liquid Al were calculated to be 1.80×10^{-9} and 3.38×10^{-9} m^2 s^{-1} in 843 K (before the nucleation of Si) respectively. It can be seen that, in Al–7Si–4Cu alloy, the diffusion of Si atoms is much more dominant than that of Cu atoms. Therefore, the local structure of melt depends on the diffusion of Si. Then, the actual dendrite tip velocity V_{dt} of Al–Si alloy is estimated by Ref. [56]:

$$V_{dt} = \frac{D\overline{m}C_L^*\left(\overline{k} - 1\right)\Delta S_V}{\pi^2\sigma}\Omega^2 \tag{9}$$

$$C_L^* = \frac{\overline{C_0}}{1 - \Omega\left(1 - \overline{k}\right)} \tag{10}$$

Note that, Eqs. (9) and (10) were deduced by assuming a hemispherical dendrite tip. In the two equations, $\overline{C_0}$, $\overline{m}$ and $\overline{k}$ are calculated by an equivalent method shown in Eqs (11-13) from Ref. [57]:

$$\overline{C_0} = \sum_{i=1}^{n} C_0^i \tag{11}$$

$$\overline{m} = \sum_{i=1}^{n} \left(m^i C_0^i\right) / \overline{C_0} \tag{12}$$

$$\overline{k} = \sum_{i=1}^{n} \left(m^i C_0^i k^i\right) / \sum_{i=1}^{n} \left(m^i C_0^i\right) \tag{13}$$

where C_0^i, m^i *and* k^i are the liquid composition, liquidus slope, and partition coefficient respectively for each alloy element in TiB_2/Al–Si-based composites. Ω is supersaturation as shown in Fig. 8(d). The parameters used in Eqs. (9) and (10) are listed as follows: m (Si) = −6.6 K/wt%, m (Cu) = −3.4 K/wt%, k (Si) = 0.117 and k (Cu) = 0.140 [56,58,59]. The calculation curve is shown in Fig. 8(f). Generally, the supersaturation of Al–Si alloy is usually lower than 0.05 [60]. So, the dendrite tip velocity is calculated to be lower than 0.48 mm/s, which is lower than the highest critical interface velocity of α-Al (95.1 mm/s). Fig. 8(f and g) compares the highest critical interface velocity V_{cr} and dendrite tip velocity V_{dt}, in which two distribution types of nanoparticles in the TiB_2/Al–Si-based composites are obtained, including the intragranular distribution ($V_{dt} > V_{cr}$, the particles are engulfed by the S/L interface and distributed within the interior of primary α-Al) and the intergranular distribution ($V_{dt} < V_{cr}$, the particles are repulsed by the S/L interface and distributed along grain boundaries). Accordingly, the dendrite tip velocity is much lower than the highest critical interface velocity of α-Al; that is, $V_{dt} < V_{cr}$. Consequently, the majority of nanoparticles in this work are pushed by the S/L interface and distributed around the α-Al dendrites to restrict their further growth.

The TEM images (Fig. 9) show the microstructures of nano/submicron-sized TiB_2/Al–Si-based composites after tensile testing at room temperature. Several submicron-sized TiB_2 particles are distributed in the interior of primary α-Al (Fig. 9(a)). The interface area "A" between TiB_2 and α-Al matrix was characterized in HRTEM, as shown in Fig. 9(b), which indicates that Al and TiB_2 have a clear and continuous interface. The Fast Fourier Transform (FTT) and Inverse Fast Fourier Transform (FTT) images of the Al matrix (area "B") and TiB_2 particles (area "C") are shown in Fig. 9 (b_1-b_4). Dislocations are evident near the TiB_2/Al interfaces in the Al matrix. This results from the mismatch of the coefficient of thermal expansion (CTE) and lattices between TiB_2 particles and Al matrix [41]. Those dislocations near the TiB_2 particles prominently promote the precipitation of θ', which is consistent with the previous discussion in Fig. 7(f). Additionally, most nanoparticles with an average size less than 80 nm are pushed by the S/L interface and distributed along grain boundaries (Fig. 9(c)), which effectively restricts the growth of α-Al dendrites. The SAED pattern in Fig. 9(c) inset also suggests that those nanoparticles are TiB_2.

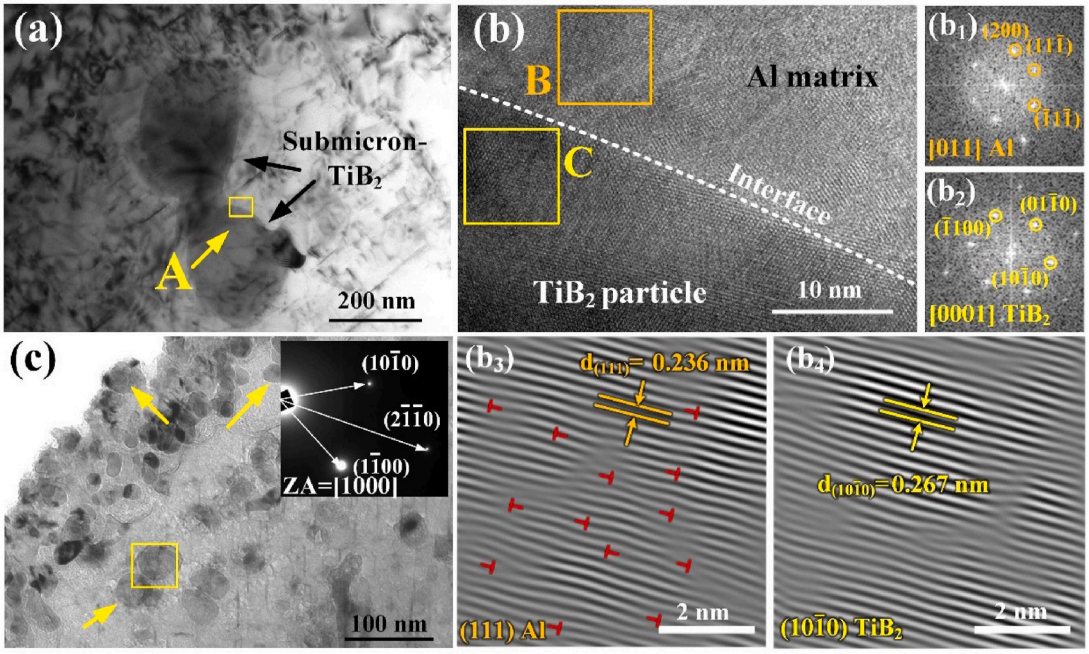

Fig. 9. TEM images of nano/submicron-sized TiB_2/Al–Si-based composites after tensile testing at room temperature: (a) TiB_2 nanoparticles distributed in the interior of primary α-Al and (b) an HRTEM image of the area "A" in (a), (c) Nano-sized TiB_2 particles distributed along α-Al grain boundaries with inset showing SAED pattern of TiB_2 particles, and the FFT images of (b_1)-(b_2) zone "B" of the Al matrix and "C" of the TiB_2 particles in (b) and (b_3)-(b_4) the IFFT image of zone "B" and "C".

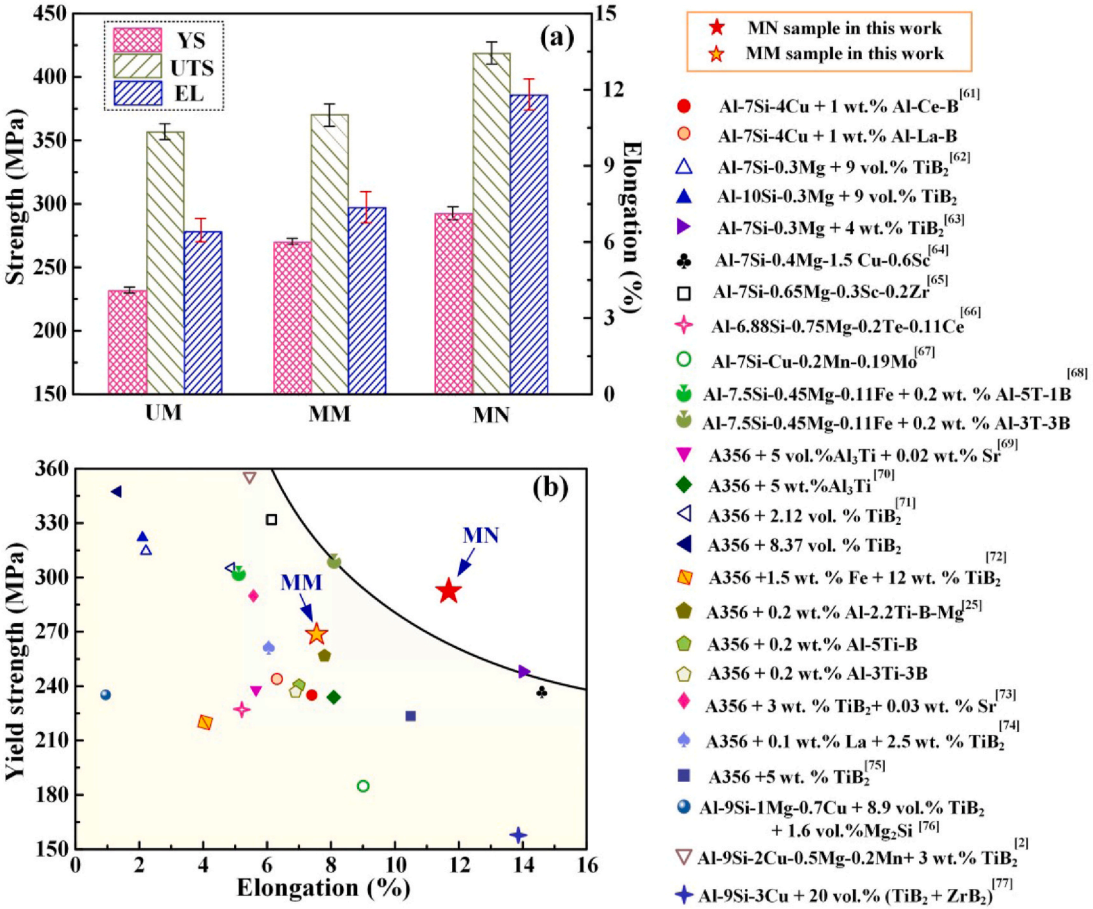

Fig. 10. (a) Tensile properties of the unmanipulated Al–Si-based alloys (UM) and the TiB_2/Al–Si-based composites manipulated by micro/submicron-sized TiB_2 particles (MM) and nano/submicron-sized TiB_2 particles (MN). (b) Comparisons between the yield strength and elongation of hypoeutectic Al–Si alloys manipulated under different treatment conditions.

3.2.4. Tailoring mechanical properties

As shown in Fig. 10(a), the yield strength (YS), ultimate tensile strength (UTS) and elongation (EL) of the TiB_2/Al–Si-based composites are simultaneously enhanced after introducing nano/submicron-sized or micron/submicron-sized TiB_2 particles. The micron/submicron-sized TiB_2 particles in TiB_2/Al–Si-based composites seem to have a relatively limited strengthening effect; YS, UTS and EL are respectively 269 MPa, 371 MPa and 8.9% for MM sample, which are 15.4%, 3.3% and 14.1% higher than the corresponding ones (233 MPa, 359 MPa and 7.8%) of UM sample. However, the nano/submicron-sized TiB_2 particles exhibit much better mechanical properties: YS, UTS and EL increase to 294 MPa, 420 MPa and 13.2% in the MN sample, which correspond to increase by 26.2%, 17.0% and 69.2%, respectively, compared with the un-manipulated sample. The simultaneous enhancement in strength and elongation is mainly ascribed to the refinement of α-Al grains, the modification of eutectic Si and the refinement of θ' precipitates induced by the hybrid-sized nano/submicron-sized TiB_2 particles. The refinement and morphology modification of eutectic Si can reduce the number of potential crack initiation sites, i.e. eutectic Si transforms from a needle-like structure in matrix alloy (UM sample) into a fine coral-like structure in tailored composites). Then, with finer α-Al grains and extended grain boundaries for effectively constraining the local deformation, microcrack initiation and propagation would be restricted. Besides, the much finer θ' precipitates induced by the introduction of nanoparticles could also strongly impede dislocation motions.

Fig. 10(b) and Table 4 show the yield strength and elongation of the hypoeutectic Al–Si alloys under different manipulation conditions. The nano/submicron-sized particles seem to have stronger strengthening effects compared to micron/submicron-sized particles and other inoculants containing Ti, B or rare earth elements. Because of no free Ti atoms in the system, further poisoning effects between Ti and Si are avoided. As such, the interface of Al/TiB_2 is clean and strong interfacial bonding is obtained. The present manipulation method by the well-designed size and morphology of TiB_2 particles in TiB_2/Al master alloys has a high potential for manipulating hypoeutectic Al–Si alloys to realize the refinement of multilevel microstructures including α-Al, eutectic Si and θ' precipitates, thereby achieving an outstanding combination of strength and ductility.

Table 4
Comparison of mechanical properties of Al–Si composites manufactured by different methods. YS: yield strength and EL: elongation.

Composition	Methods	YS (MPa)	EL (%)	Ref.
Al–7Si–4Cu	0.7 wt% Micro-/submicro-TiB_2	269	8.9	In this work
	0.7 wt% Nano-/submicro-TiB_2	294	13.2	
Al–7Si–4Cu	1 wt% Al–Ce–B	243	6.3	[61]
	1 wt% Al–La–B	235	7.4	
Al–7Si-0.3 Mg	9 vol%TiB_2 (LPDC)	314	2.2	[62]
Al–10Si-0.3 Mg	9 vol% TiB_2 (LPDC)	322	2.1	
Al–7Si-0.3 Mg	4 wt% TiB_2	250	14.0	[63]
Al–7Si-0.4Mg-1.5Cu	0.6 wt% Sc	237	14.6	[64]
Al–7Si-0.65 Mg	0.3 wt% Sc + 0.2 wt% Zr	330	6.1	[65]
Al-6.88Si-0.75 Mg	0.2 wt% Te + 0.11 wt% Ce	227	5.7	[66]
Al–7Si–Cu-0.2Mn	0.19 wt% Mo	185	9.0	[67]
Al-7.5Si-0.45Mg-0.11Fe	0.2 wt% Al–5Ti–B	299	4.5	[68]
	0.2 wt% Al–3Ti–3B	305	8.5	
A356	5 vol% Al_3Ti + 0.22 wt% Sr	238	6.4	[69]
A356	5 wt% Al_3Ti	234	8.6	[70]
A356	2.12 vol% TiB_2	305	4.9	[71]
	4.66 vol% TiB_2	317	1.9	
	8.37 vol% TiB_2	347	1.3	
A356	1.5 wt% Fe + 12 wt% TiB_2	223	3.9	[72]
A356	0.2 wt% Al-2.2Ti–B–Mg	257	7.8	[25]
	0.2 wt% Al–5Ti–B	241	6.5	
	0.2 wt% Al–3Ti–3B	240	6.4	
A356	3 wt% TiB_2 + 0.03 wt% Sr	260	5.6	[73]
A356	2.5 wt% TiB_2 + 0.1 wt% La	261	6.0	[74]
A356	5 wt% TiB_2	223	10.5	[75]
Al–9Si–1Mg-0.7Cu	8.9 vol% TiB_2 + 1.6 vol % Mg_2Si	235	1.2	[76]
Al–9Si–2Cu-0.5Mg-0.2Mn	3 wt% TiB_2 (HPDC)	356	5.5	[2]
Al–9Si–3Cu	20 vol% (TiB_2 + ZrB_2)	265	14.8	[77]

4. Conclusion

This work proposed an in-situ synthesis strategy by combustion synthesis in Al–Ti–B reaction system to elaborately tune the size, morphology and crystallographic terminated planes of TiB_2 particles in TiB_2/Al precursors. Furthermore, the designed TiB_2 reinforced Al–Si-based composites were constructed and were found to exhibit enhanced strength-ductility synergy.

(1) As the Al content or B/Ti ratio increases, the average size of TiB_2 particles synthesized from the Al–Ti–B system decreases. When the B/Ti ratio is 2.4, the final 20 wt% TiB_2/Al precursor consists of only Al matrix and Ti-terminated TiB_2, and the as-synthesized TiB_2 particles are predominantly in nanoscale with near-spherical morphology and in submicron-scale with hexagonal morphology.
(2) During the manipulation of Al–Si–Cu-based alloy by different size of TiB_2 particles, the submicron-sized TiB_2 particles are more likely to serve as α-Al heterogeneous nucleation sites or dissolve into α-Al dendrites, while the nano-sized TiB_2 is repulsed to the solid/liquid (S/L) interface and physically restricts the growth of the α-Al dendrites. Hereinto, Al/TiB_2 and Si/TiB_2 interfaces also exhibit good interfacial bonding with low lattice mismatch.
(3) Nano/submicron-sized TiB_2 particles can significantly manipulate the microstructures of the Al–Si–Cu-based composites. Primary α-Al dendrites, eutectic Si and θ' precipitates of the are substantially refined by 79.2%, 51.9% and 37.6% respectively compared with the corresponding ones in the unmanipulated Al–Si–Cu-based alloy.
(4) By optimizing the spatial distribution of TiB_2 particles in the Al matrix, the yield strength, ultimate tensile strength and elongation of the nano/submicron-sized TiB_2 particles reinforced Al–Si–Cu-based composites are simultaneously increased by 26.2%, 17.0% and 69.2% compared with the unmanipulated Al–Si–Cu-based alloy.
(5) The nano/submicron-sized TiB_2 particles in the Al–Si-based alloy perform superior refinement and strengthening effects than the micro/submicron-sized TiB_2 particles or TiB_2 particles synthesized by other methods.

As such, this work provides a novel manipulative strategy for high-performance Al–Si-based composites, which breaks through the inherent strength-ductility trade-off limitation of conventional fabrication methods and obtains an outstanding combination of strength and ductility in Al–Si-based composites.

Authorship contribution statement

Bai-Xin Dong: Conceptualization, Formal analysis, Experiment, Writing-original draft. **Qiang Li** and **Zhi-Fa Wang**: Formal analysis, Validation and Experiment. **Tian-Shu Liu and Liang-Yu Chen:** Conceptualization, Validation, Experiment. **Hong-Yu Yang:** Conceptualization, Writing-review and editing. **Shi-Li Shu:** Formal analysis, Writing-review and editing. **Feng Qiu:** Macro-scale simulation, Validation, Writing-review and editing. **Qi-Chuan Jiang:** Supervision, Writing-review and editing. **Lai-Chang Zhang:** Conceptualization,

Formal analysis, Writing-review and editing.

Declaration of competing interest

The authors declare that they have no known competing financial interests or personal relationships that could have appeared to influence the work reported in this paper.

Acknowledgements

This work was supported by National Natural Science Foundation of China (No. 51771081 and No. 51971101), the 'thirteenth five-year plan' Science & Technology Research Foundation of Education Bureau of Jilin Province, China (Grant No. JJKH20200971KJ), the Science and Technology Development Program of Jilin Province, China (20190302004GX), the Postdoctoral Science Foundation of China (No. 2020M670849), and the Graduate Innovation Fund of Jilin University (No. 101832020CX139).

References

[1] Gao YY, Qiu F, Geng R, Chu JG, Zhao QL, Jiang QC. Effects of nanosized TiC_p dispersion on the high-temperature tensile strength and ductility of in situ TiC_p/Al-Cu-Mg-Si nanocomposites. J Alloys Compd 2019;774:425–33.
[2] Dong X, Youssef H, Zhang Y, Wang S, Ji S. High performance Al/TiB_2 composites fabricated by nanoparticle reinforcement and cutting-edge super vacuum assisted die casting process. Compos B Eng 2019;177:107453.
[3] Dong B-X, Yang H-Y, Qiu F, Li Q, Shu S-L, Zhang B-Q, et al. Design of TiC nanoparticles and their morphology manipulating mechanisms by stoichiometric ratios: Experiment and first-principle calculation. Mater Des 2019;181:107951.
[4] Liu S, Han S, Zhang L, Chen LY, Wang L, Zhang L, et al. Strengthening mechanism and micropillar analysis of high-strength NiTi-Nb eutectic-type alloy prepared by laser powder bed fusion. Compos B Eng 2020;200:108358.
[5] Wang L, Lu W, Hu Q, Xia M, Wang Y, Li J guo. Interfacial tuning for the nucleation of liquid AlCu alloy. Acta Mater 2017;139:75–85.
[6] Huang LJ, Geng L, Peng HX. Microstructurally inhomogeneous composites: is a homogeneous reinforcement distribution optimal? Prog Mater Sci 2015;71:93–168.
[7] Reddy MP, Manakari V, Parande G, Shakoor RA, Mohamed AMA, Gupta M. Structural, mechanical and thermal characteristics of Al-Cu-Li particle reinforced Al-matrix composites synthesized by microwave sintering and hot extrusion. Compos B Eng 2019;164:485–92.
[8] Zhang X, Chen T, Ma S, Qin H, Ma J. Overcoming the strength-ductility trade-off of an aluminum matrix composite by novel core-shell structured reinforcing particulates. Compos B Eng 2021;206:108541.
[9] Han T, Wang F, Li J, Zhao N, He C. Simultaneously enhanced strength and ductility of Al matrix composites through the introduction of intragranular nano-sized graphene nanoplates. Compos B Eng 2021;212:108700.
[10] Qiu D, Taylor JA, Zhang M-X, Kelly PM. A mechanism for the poisoning effect of silicon on the grain refinement of Al-Si alloys. Acta Mater 2007;55:1447–56.
[11] Li Y, Hu B, Liu B, Nie A, Gu Q, Wang J, et al. Insight into Si poisoning on grain refinement of Al-Si/Al-5Ti-B system. Acta Mater 2020;187:51–65.
[12] Li Y, Jiang Y, Liu B, Luo Q, Hu B, Li Q. Understanding grain refining and anti Si-poisoning effect in Al-10Si/Al-5Nb-B system. J Mater Sci Technol 2021;65:190–201.
[13] Wang K, Jiang HY, Jia YW, Zhou H, Wang QD, Ye B, et al. Nanoparticle-inhibited growth of primary aluminum in Al-10Si alloys. Acta Mater 2016;103:252–63.
[14] Xu Y, Casari D, Du Q, Mathiesen RH, Arnberg L, Li Y. Heterogeneous nucleation and grain growth of inoculated aluminium alloys: an integrated study by in-situ X-radiography and numerical modelling. Acta Mater 2017;140:224–39.
[15] Prasad A, Yuan L, Lee PD, Stjohn DH. The Interdependence model of grain nucleation: a numerical analysis of the Nucleation-Free Zone. Acta Mater 2013;61:5914–27.
[16] Li B, Xu K, Chen R, Li Y, Wang X, Jiang C, et al. On the fatigue crack propagation mechanism of a TiB_2-reinforced high-modulus steel. Compos B Eng 2020;190:107960.
[17] Wang P, Gammer C, Brenne F, Niendorf T, Eckert J, Scudino S. A heat treatable TiB_2/Al-3.5Cu-1.5Mg-1Si composite fabricated by selective laser melting: microstructure, heat treatment and mechanical properties. Compos B Eng 2018;147:162–8.
[18] Xiao P, Gao Y, Yang C, Li Y, Huang X, Liu Q, et al. Strengthening and toughening mechanisms of Mg matrix composites reinforced with specific spatial arrangement of in-situ TiB_2 nanoparticles. Compos B Eng 2020;198:108174.
[19] Li Q, Qiu F, Dong BX, Gao X, Shu SL, Yang HY, et al. Processing, multiscale microstructure refinement and mechanical property enhancement of hypoeutectic Al-Si alloys via in situ bimodal-sized TiB_2 particles. Mater Sci Eng, A 2020;777:139081.
[20] Xie X, Chen C, Chen Z, Wang W, Yin S, Ji G, et al. Achieving simultaneously improved tensile strength and ductility of a nano-TiB_2/AlSi10Mg composite produced by cold spray additive manufacturing. Compos B Eng 2020;202:108404.
[21] Deng C, Xu B, Wu P, Li Q. Stability of the Al/TiB_2 interface and doping effects of Mg/Si. Appl Surf Sci 2017;425:639–45.
[22] Wang Q, Liu C, Yao R, Zhu H, Liu X, Wang M, et al. First-principles study on the stability and work function of low-index surfaces of TiB_2. Comput Mater Sci 2020;172:109356.
[23] Fan Z, Wang Y, Zhang Y, Qin T, Zhou XR, Thompson GE, et al. Grain refining mechanism in the Al/Al-Ti-B system. Acta Mater 2015;84:292–304.
[24] Greer AL, Bunn AM, Tronche A, Evans PV, Bristow DJ. Modelling of inoculation of metallic melts: application to grain refinement of aluminium by Al-Ti-B. Acta Mater 2000;48:2823–35.
[25] Zhang Y, Ji S, Fan Z. Improvement of mechanical properties of Al-Si alloy with effective grain refinement by in-situ integrated Al2.2Ti1B-Mg refiner. J Alloys Compd 2017;710:166–71.
[26] Stjohn DH, Qian M, Easton MA, Cao P. The Interdependence Theory: the relationship between grain formation and nucleant selection. Acta Mater 2011;59:4907–21.
[27] Mohanty PS, Gruzleski JE. Grain refinement mechanisms of hypoeutectic Al-Si alloys. Acta Mater 1996;44:3749–60.
[28] Han YF, Dai YB, Wang J, Shu D, Sun BD. First-principles calculations on Al/AlB_2 interfaces. Appl Surf Sci 2011;257:7831–6.
[29] Zhang HL, Han YF, Wang J, Dai YB, Sun BD. An ab initio molecular dynamics study on the structural and electronic properties of AlB_2, TiB_2 and $(Al_x,Ti_{(1-x)})B_2$ in Al-Ti-B master alloys. J Alloys Compd 2014;585:529–34.
[30] Zhang HL, Han YF, Dai YB, Wang J, Sun BD. An ab initio molecular dynamics study: liquid-Al/solid-TiB_2 interfacial structure during heterogeneous nucleation. J Phys D Appl Phys 2012;45:455307.
[31] Wearing D, Horsfield AP, Xu W, Lee PD. Which wets TiB_2 inoculant particles: Al or Al_3Ti? J Alloys Compd 2016;664:460–8.
[32] Chen LY, Xu JQ, Choi H, Konishi H, Jin S, Li XC. Rapid control of phase growth by nanoparticles. Nat Commun 2014;5:1–9.
[33] Wang K, Jiang H, Wang QD, Ye B, Ding W. A novel method to achieve grain refinement in aluminum. Metall Mater Trans A Phys Metall Mater Sci 2016;47:4788–94.
[34] Ma X, Zhao YF, Tian WJ, Qian Z, Chen HW, Wu YY, et al. A novel Al matrix composite reinforced by nano-AlN_p network. Sci Rep 2016;6:34919.
[35] Guo E, Shuai S, Kazantsev D, Karagadde S, Phillion AB, Jing T, et al. The influence of nanoparticles on dendritic grain growth in Mg alloys. Acta Mater 2018;152:127–37.
[36] Cao C, Yao G, Jiang L, Sokoluk M, Wang X, Ciston J, et al. Bulk ultrafine grained/nanocrystalline metals via slow cooling. Sci Adv 2019;5:eaaw2398.
[37] Zan YN, Zhou YT, Zhao H, Liu ZY, Wang QZ, Wang D, et al. Enhancing high-temperature strength of (B_4C+Al_2O_3)/Al designed for neutron absorbing materials by constructing lamellar structure. Compos B Eng 2020;183:1–11.
[38] Jin S, Shen P, Li Y, Zhou D, Jiang Q. Synthesis of spherical NbB_{2-x} particles by controlling the stoichiometry. CrystEngComm 2012;14:1925.
[39] Yang H-Y, Wang Z, Chen L-Y, Shu S-L, Qiu F, Zhang L-C. Interface formation and bonding control in high-volume-fraction (TiC+TiB_2)/Al composites and their roles in enhancing properties. Compos B Eng 2021;209:108605.
[40] Tian W, Zhao Q, Geng R, Qiu F, Jiang Q. Improved creep resistance of Al-Cu alloy matrix composite reinforced with bimodal-sized TiC_p. Mater Sci Eng, A 2018;713:190–4.
[41] Gao YY, Dong BX, Qiu F, Geng R, Wang L, Zhao QL, et al. The superior elevated-temperature mechanical properties of Al-Cu-Mg-Si composites reinforced with in situ hybrid-sized TiC_x-TiB_2 particles. Mater Sci Eng, A 2018;728:157–64.
[42] Nafisi S, Ghomashchi R. Grain refining of conventional and semi-solid A356 Al-Si alloy. J Mater Process Technol 2006;174:371–83.
[43] Emamy M, Mahta M, Rasizadeh J. Formation of TiB_2 particles during dissolution of $TiAl_3$ in Al-TiB_2 metal matrix composite using an in situ technique. Compos Sci Technol 2006;66:1063–6.
[44] Wang T, Fu H, Chen Z, Xu J, Zhu J, Cao F, et al. A novel fading-resistant Al-3Ti-3B grain refiner for Al-Si alloys. J Alloys Compd 2012;511:45–9.
[45] Li P, Wu Y, Liu X. Controlled synthesis of different morphologies of TiB_2 microcrystals by aluminum melt reaction method. Mater Res Bull 2013;48:2044–8.
[46] Song S, Zhang T, Xie C, Zhou J, Li R, Zhen Q. Growth behavior of TiB_2 hexagonal plates prepared via a molten-salt-mediated carbothermal reduction. J Am Ceram Soc 2020;103:719–23.
[47] Wang F, Qiu D, Liu ZL, Taylor JA, Easton MA, Zhang MX. The grain refinement mechanism of cast aluminium by zirconium. Acta Mater 2013;61:5636–45.
[48] Zhu L, Qiu F, Qiu D, Duan TT, Chang F, Li TT, et al. Efficient microstructure refinement of Al-Si-Mg alloy manipulated by nanocrystals formed by in-situ crystallization in melt. Mater Sci Eng, A 2019;751:90–8.
[49] Zhang M, Kelly P, Easton M, Taylor J. Crystallographic study of grain refinement in aluminum alloys using the edge-to-edge matching model. Acta Mater 2005;53:1427–38.
[50] Yang Q, Ma Y, Chen Z, Ji G, Wang ML, Zhong SY, et al. A new powder metallurgy routine to fabricate TiB_2/Al-Zn-Mg-Cu nanocomposites based on composite powders with pre-embedded nanoparticles. Materialia 2019;8:100458.
[51] Youssef YM, Dashwood RJ, Lee PD. Effect of clustering on particle pushing and solidification behaviour in TiB_2 reinforced aluminium PMMCs. Compos Part A Appl Sci Manuf 2005;36:747–63.
[52] David R Lide E. CRC handbook of chemistry and physics. 87th Edition. Taylor Fr Boca Rat FL; 2007. Internet Version 2007.
[53] Song X, Bian X, Zhang J, Zhang J. Temperature-dependent viscosities of eutectic Al-Si alloys modified with Sr and P. J Alloys Compd 2009;479:670–3.
[54] Abrikosov AA, Letterson JB. Introduction to the theory of normal metals. Phys Today 1973;26:55–6.

[55] Du Q, Li YJ. Prediction of as-cast grain size of inoculated multicomponent aluminum alloys. Mater Sci Forum 2014;790–791:185–90.
[56] Greer AL. Overview: application of heterogeneous nucleation in grain-refining of metals. J Chem Phys 2016;145:211704.
[57] Xu J, Li Y, Ma K, Fu Y, Guo E, Chen Z, et al. In-situ observation of grain refinement dynamics of hypoeutectic Al-Si alloy inoculated by Al-Ti-Nb-B alloy. Scripta Mater 2020;187:142–7.
[58] Shu D, Sun B, Mi J, Grant PS. A quantitative study of solute diffusion field effects on heterogeneous nucleation and the grain size of alloys. Acta Mater 2011;59:2135–44.
[59] Du Q, Li Y. An extension of the Kampmann-Wagner numerical model towards as-cast grain size prediction of multicomponent aluminum alloys. Acta Mater 2014;71:380–9.
[60] Wang K, Jiang HY, Jia YW, Zhou H, Wang QD, Ye B, et al. Nanoparticle-inhibited growth of primary aluminum in Al-10Si alloys. Acta Mater 2016;103:252–63.
[61] Jing L, Pan Y, Lu T, Chai W. Refinement effect of two rare earth borides in an Al-7Si-4Cu alloy: a comparative study. Mater Char 2018;145:664–70.
[62] Ji S, Amirkhanlu F, Mostaed A, Beanland R. Atomic structure and interface chemistry in a high-stiffness and high-strength Al-Si-Mg/TiB_2 nanocomposite. Mater Sci Eng, A 2019;763:138072.
[63] Wang T, Chen Z, Zheng Y, Zhao Y, Kang H, Gao L. Development of TiB_2 reinforced aluminum foundry alloy based in situ composites - Part II : enhancing the practical aluminum foundry alloys using the improved Al - 5 wt % TiB_2 master composite upon dilution. Mater Sci Eng, A 2014;605:22–32.
[64] Xu C, Ma C, Sun Y, Hanada S, Lu G, Guan S. Optimizing strength and ductility of Al-7Si-0.4 Mg foundry alloy: role of Cu and Sc addition. J Alloys Compd 2019;810:151944.
[65] Xu C, Xiao W, Zheng R, Hanada S, Yamagata H, Ma C. The synergic effects of Sc and Zr on the microstructure and mechanical properties of Al-Si-Mg alloy. Mater Des 2015;88:485–92.
[66] Kang J, Su R, Wu DY, Liu CH, Li T, Wang LS, et al. Synergistic effects of Ce and Mg on the microstructure and tensile properties of Al-7Si-0.3Mg-0.2Fe alloy. J Alloys Compd 2019;796:267–78.
[67] Shaha SK, Czerwinski F, Kasprzak W, Friedman J, Chen DL. Ageing characteristics and high-temperature tensile properties of Al-Si-Cu-Mg alloys with micro-additions of Mo and Mn. Mater Sci Eng, A 2017;684:726–36.
[68] Dong X, Ji S. Si poisoning and promotion on the microstructure and mechanical properties of Al-Si-Mg cast alloys. J Mater Sci 2018;53:7778–92.
[69] Ma S, Wang X. Mechanical properties and fracture of in-situ Al_3Ti particulate reinforced A356 composites. Mater Sci Eng, A 2019;754:46–56.
[70] Yang C, Liu Z, Zheng Q, Cao Y, Dai X, Sun L, et al. Ultrasound assisted in-situ casting technique for synthesizing small-sized blocky Al_3Ti particles reinforced A356 matrix composites with improved mechanical properties. J Alloys Compd 2018;747:580–90.
[71] Wang T, Zheng Y, Chen Z, Zhao Y, Kang H. Effects of Sr on the microstructure and mechanical properties of in situ TiB_2 reinforced A356 composite. Mater Des 2014;64:185–93.
[72] Lin B, Li H, Xu R, Shi Y, Xiao H, Zhang W, et al. Precipitation of iron-rich intermetallics and mechanical properties of Al-Si-Mg-Fe alloys with Al-5Ti-B. Mater Sci Technol 2018;34:2145–52.
[73] Wang T, Zheng Y, Chen Z, Zhao Y, Kang H. Effects of Sr on the microstructure and mechanical properties of in situ TiB_2 reinforced A356 composite. Mater Des 2014;64:185–93.
[74] Wang T, Zhao Y, Chen Z, Zheng Y, Kang H. Combining effects of TiB_2 and La on the aging behavior of A356 alloy. Mater Sci Eng, A 2015;644:425–30.
[75] Liu Z, Dong Z, Cheng X, Zheng Q, Zhao J, Han Q. On the supplementation of magnesium and usage of ultrasound stirring for fabricating in situ TiB_2/A356 composites with improved mechanical properties. Metall Mater Trans A 2018;49:5585–98.
[76] Amirkhanlou S, Ji S, Zhang Y, Watson D, Fan Z. High modulus Al-Si-Mg Cu/Mg_2Si-TiB_2 hybrid nanocomposite: microstructural characteristics and micromechanics-based analysis. J Alloys Compd 2017;694:313–24.
[77] Zhang SL, Shi XX, Zhao YT, Zhang BR, Liang ZP, Yin HS, et al. Preparation, microstructures and mechanical properties of in-situ (TiB_2+ ZrB_2)/AlSi9Cu3 composites. J Alloys Compd 2016;673:349–57.